Confinement improvement during detached phase with RMP application in deuterium plasmas of LHD

PAPER • OPEN ACCESS

Confinement improvement during detached phase with RMP application in deuterium plasmas of LHD

To cite this article: M. Kobayashi *et al* 2022 *Nucl. Fusion* **62** 056006

View the article online for updates and enhancements.

Confinement improvement during detached phase with RMP application in deuterium plasmas of LHD

M. Kobayashi[1,2,*] ⃝, **R. Seki**[1], **Y. Hayashi**[1] ⃝, **T. Oishi**[1,2], **K. Tanaka**[1,3],
Y. Takemura[1] ⃝, **K. Ida**[1,2] ⃝, **T. Kinoshita**[3] ⃝, **K. Mukai**[1] ⃝, **S. Morita**[1]
and S. Masuzaki[1,2] ⃝

[1] National Institute for Fusion Science, National Institutes of Natural Sciences, Toki, Gifu 509-5292, Japan
[2] National Institute for Fusion Science, SOKENDAI, The Graduate University for Advanced Studies,
Toki, Gifu, 509-5292, Japan
[3] Interdisciplinary Graduate School of Engineering Sciences, Kyushu University, Kasuga, Fukuoka,
816-8580, Japan

E-mail: kobayashi.masahiro@nifs.ac.jp

CrossMark

Abstract

In order to explore the compatibility of good core plasma performance with divertor heat load
mitigation, the interaction between cold edge plasma and core plasma transport, including the
edge transport barrier (ETB), has been analysed in the divertor detachment discharges of
deuterium plasmas in LHD with resonant magnetic perturbation (RMP) field application. The
RMP application introduces a widened edge stochastic layer and sharp boundary in the
magnetic field structure between the confinement region and the edge stochastic layer. The
widened edge stochastic layer enhances impurity radiation and provides stable detachment
operation as compared with the case without RMP. It is found that ETB is formed at the
confinement boundary at the onset of detachment transition. However, as the detachment
deepens, the resistive pressure gradient-driven MHD mode is excited, which degrades the
ETB. At the same time, however, the core transport decreases to keep global plasma stored
energy (W_p) unchanged, showing clear core-edge coupling. After a gradual increase of density
fluctuation during the MHD activity, a spontaneous increase of W_p and the recovery of ETB
are observed while the detachment is maintained. Then, the coherent MHD mode ceases and
ELM-like bursts appear. In the improved mode, impurity decontamination occurs, and the
divertor heat load increases slightly. Key controlling physical processes in the interplay
between core and cold edge plasma are discussed. A comparison between deuterium and
hydrogen plasmas shows that hydrogen plasmas exhibit similar features to the deuterium ones
in terms of density and magnetic fluctuations, impurity decontamination towards higher
confinement, etc. But most of the features are modest in the hydrogen plasmas and thus no
clear confinement mode transition with clear ETB formation is defined. Better global

confinement is obtained in the deuterium plasmas than the hydrogen ones at a higher radiation level.

(Some figures may appear in colour only in the online journal)

1. Introduction

The compatibility of good core plasma performance with divertor heat load mitigation is a critical issue in the realizisation of a nuclear fusion reactor. In general, core confinement tends to degrade with increasing impurity radiation. In highly radiative plasmas, where the edge temperature is lowered to enhance the impurity radiation, there are several key physical processes that affect the core confinement. Deterioration of the edge transport barrier (ETB) is considered, caused by decreasing adiabaticity with the reduction of edge temperature. The adiabaticity parameter is defined as $\alpha_{adi} = k_{\parallel}^2 v_{th}^2 / (\nu_{ei} |\omega|)$, which is a ratio of the parallel electron diffusion rate and turbulence propagation speed of the dominant mode. It has a parameter dependence of $\alpha_{adi} \propto T_e^{2.5}/n$, thus it decreases with temperature. The reduction of α_{adi} leads to an increase of drift wave turbulence transport [1]. On the other hand, the reduced edge temperature can also reach an instability threshold of resistive pressure gradient-driven MHD instability, such as interchange and ballooning modes. The growth rate of the mode has a parameter dependency of $\gamma \propto L_p^{-2/3} T_e^{-0.5}$, and therefore the lower the temperature, the easier it is to excite. The excitation of the mode can degrade the transport barrier significantly [2, 3]. A parameter to characterize the transition of the transport is proposed as $\alpha_{dia} = (R/2L_n)^{0.25} \sqrt{D_{gB}/D_{DRB}}$, which is interpreted as a ratio of drift wave frequency and resistive ballooning mode growth rate, and has a parameter dependence of $\alpha_{dia} \propto T_e/\sqrt{n}$.

In addition to these effects on ETB, impurity influx to the confinement region provides complex effects on the core performance. It dilutes the fuel species and decreases the fusion reaction rate. The impurity in the core region also cools the plasma via impurity radiation. At the same time, however, the impurity may act as suppression of turbulence in some modes [4]. There might be an optimum quantity of impurity in a balance between these processes [5, 6].

On the other hand, the establishment of ETB, which is a signature of H-mode confinement, is a bifurcation phenomenon and occurs spontaneously when the plasma reaches a transition threshold [7, 8]. The divertor detachment is also a bifurcation process in terms of an energy balance between power input and loss channels, the latter of which are the energy transport loss to divertor plates as well as impurity radiation. Both of the processes have strong nonlinearity with respect to temperature, resulting in bifurcation between high and low temperature branches [9]. Therefore, the realization of compatibility between the good core confinement and divertor heat load mitigation with detachment is to search for an operating regime, where the branches in both of the bifurcations are satisfied with the ETB formation and the low edge temperature simultaneously. It is noted that the plasma parameter dependences of α_{adi} and α_{dia} are different from each other. Thus, the two mechanisms can impose different boundary conditions for the operating regime. In addition to that, during the detachment operation, the radiating edge layer has to be stabilized to prevent it from penetrating the confinement region. This is determined by competition between the thermal condensation instability growth rate, its propagation speed in the nonlinear phase, and impurity confinement time, etc. The integration of the core plasma performance and divertor heat load mitigation is realized with an understanding of these physical processes and the interplay between them.

Among these issues, in this paper, we focus on the interaction between the cold edge plasma and ETB during the detachment observed in the large helical device (LHD). The resonant magnetic perturbation (RMP) field is utilized to change the edge magnetic field structure to study its effects on the core confinement and impurity radiation. In the previous study with hydrogen plasmas, it was found that the RMP enhances impurity radiation with increased low temperature volume, and is effective in stabilizing the edge radiation layer [10–14]. In the present experiments in deuterium plasmas, it is newly discovered that a steep edge pressure gradient is formed immediately at the boundary of the confinement region with the onset of plasma detachment with the RMP application. Deterioration of the ETB occurs with the excitation of the MHD mode due to a lowering of the edge temperature as the detachment deepens, while the adiabaticity parameter is still high. The core transport responds to compensate for the ETB degradation. As a consequence, the plasma stored energy is maintained. After a substantial increase in density fluctuation, a spontaneous increase of plasma stored energy and recovery of ETB occurs during the detached phase. These observations are important to consider the mechanism of the interplay between core confinement and cold edge plasmas, and provide a possible route for the realization of divertor heat load mitigation compatible with good core performance.

The rest of the paper is organized as follows. In section 2, the edge magnetic field structure of the LHD and its impact on the plasma performance, for example, radiated power and core confinement, are presented, with and without RMP application, for comparison. In section 3, we focus on the confinement mode transition observed during detachment in deuterium plasmas with RMP application, as well as impurity
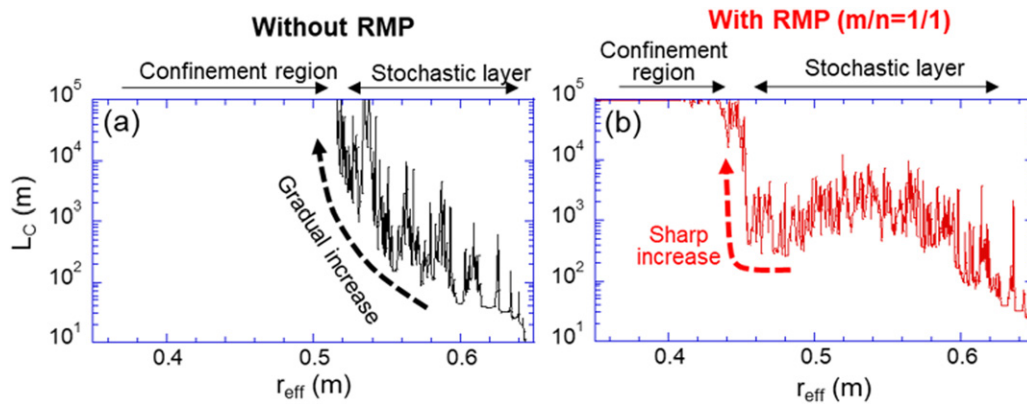
Figure 1. Radial profiles of magnetic field line connection length (L_C) (*a*) without RMP, and (*b*) with RMP application.

behaviour and divertor heat load pattern. In section 4, a comparison between deuterium and hydrogen plasmas is made. Section 5 summarizes the paper.

2. Difference in core and divertor plasmas with and without an RMP field

2.1. Change of edge magnetic field structure by applying an RMP field

An LHD is a heliotron type device with a major radius of 3.9 m and an averaged minor radius of ∼0.6 m [15]. A set of superconducting helical coils and poloidal coils creates a confinement magnetic field with a poloidal winding number of $l = 2$ and a toroidal field period of $n = 10$ [16]. The edge region is surrounded by a stochastic magnetic layer created by overlapping magnetic islands caused by different mode spectrums of the intrinsic magnetic field. The magnetic configuration in the experiments is magnetic axis (R_{ax}) = 3.90 m and a magnetic field strength of 2.54 T, respectively. An RMP of $m/n = 1/1$ mode ($B_r/B_0 \sim 0.1\%$) was applied by a set of perturbation coils installed at the top and bottom of the torus. The RMP induces a remnant island structure at a radius of rotational transform = 1, which is located at the last closed flux surface of an unperturbed equilibrium field in this magnetic field configuration. As shown in [10, 17], if the island location moves radially inward, the detachment stabilization is not obtained, but instead the divertor detachment is often accompanied by radiation collapse. It is, therefore, important to locate the island at the region with open field lines to effectively affect the impurity radiation.

Figure 1 shows the radial profiles of the magnetic field connection length (L_C) for the cases with and without RMP. r_{eff} is defined as a radius of a cylinder that encloses the plasma volume inside the flux surface. The magnetic field line was traced up to 10^5 m. In the case without RMP, L_C is in the range of 10^2 10^4 m in the stochastic layer. It gradually increases towards the inner radii, and finally reaches 10^5 m, the region which is considered as a confinement region. By applying RMP, a wide radial range filled with L_C of 10^3 m appears. This is a consequence of the formation of a magnetic island which is, however, stochastized and has no clear separatrix. In the present analysis, we call this region (the remnant island) stochastic layer. A sharp boundary appears between the confinement

region and stochastic layer. The boundary corresponds to the inner separatrix of the remnant island. As shown in the next section, the change of the edge magnetic field structure results in a significant difference in the performance of the core and divertor plasmas.

2.2. Core and divertor plasmas with and without an RMP field

Figure 2 shows the temporal evolutions of plasma parameters in density ramp-up discharges with and without RMP application in deuterium plasmas. The plasma was heated by tangential NBI with an injection energy of 152–177 keV (3.6 MW in the co-direction and 1.4 MW in the counter-direction, respectively). The density was ramped up by a deuterium gas puff. The radiating impurity was carbon originating from the graphite divertor plates, without additional impurity seeding. The density limit derived from Sudo scaling [18] is shown with dashed lines in figures 2(*a*) and (*f*). Without RMP, the density can be increased only up to 80% of the density limit. Further gas fuelling leads to radiation collapse, as shown in the figure. The divertor particle flux saturates around 4 s and starts to decrease just before the collapse. The result shows difficulty in stable detachment control without RMP. In the case with RMP application, the divertor particle flux reduction occurs at 3.95 s, indicating detachment transition. The detached phase is sustained stably up to 5.15 s. The density can be increased more than the density limit. The radiated power is enhanced up to ∼60% of the input power, which is significantly larger than the case without RMP, where the radiated power remains at ∼30% in the steady state phase. The plasma stored energy, W_p, is also larger with RMP than without RMP. There is a spontaneous increase in W_p at 3.95 and 4.5 s (figure 2(*h*)), which is considered to be caused by confinement mode transition, as discussed later. Pressure gradient profiles are plotted in figures 2(*e*) and (*j*), where the clear development of a steep gradient is confirmed in the case with RMP. The ETB location corresponds to the sharp boundary of the confinement region ($r_{eff} \sim +/-0.45$ m), as shown in figure 1(*b*). During the pressure profile steepening, spikes in the divertor particle flux appear, caused by ELM activity. The loss of plasma stored energy due to the ELM is about 3%–4%. In the case without RMP, the pressure gradient tends
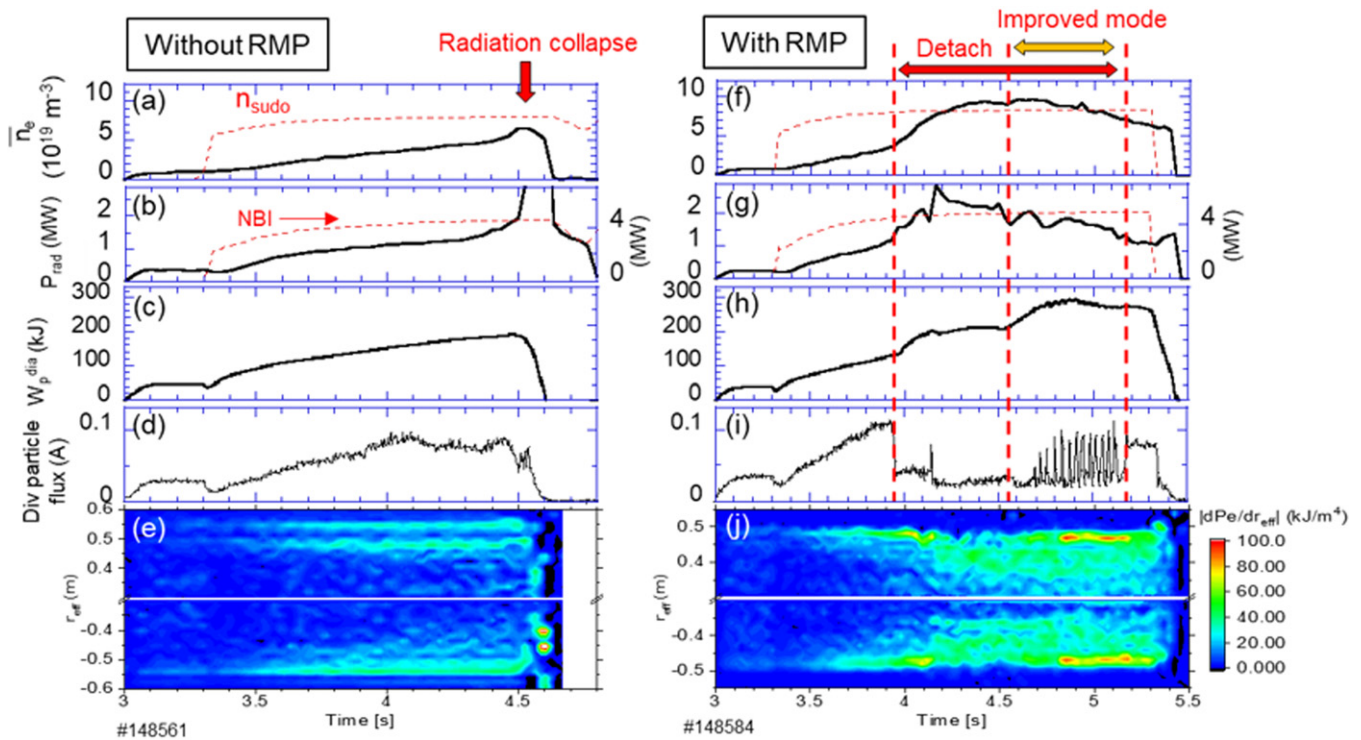
Figure 2. Time traces of (*a*) and (*f*) line-averaged density and density limit (dashed line), (*b*) and (*g*) radiated power and NBI power (dashed line), (*c*) and (*h*) plasma stored energy (W_p), (*d*) and (*i*) divertor particle flux, (*e*) and (*j*) pressure gradient. Left column: without RMP, right column: with RMP. (Data from deuterium plasmas.)

to increase at the edge region, too, as shown in figure 2(*e*). But the gradient is low as compared to the case with RMP.

Figure 3 shows the radial profiles of edge electron density (n_e) and temperature (T_e) for different line averaged densities, 3.0×10^{19} m^{-3} in figures 3(*a*) and (*e*) and 6.6×10^{19} m^{-3} in figures 3(*b*) and (*f*), respectively. Electron pressure (P_e) profiles are shown in figures 3(*c*) and (*g*) for the corresponding timings in figures 3(*a*), (*b*), (*e*) and (*f*). L_C profiles are shown figures 3(*d*) and (*h*). The left (figures 3(*a*)–(*d*)) and right (figures 3(*e*)–(*h*)) panels are for the cases without and with RMP, respectively. In the attached phase with RMP application, clear flattening of T_e appears at the widened edge stochastic layer, and a sharp increase occurs at the confinement boundary, where L_C also increases sharply, as shown in figures 3(*e*) and (*h*). In the n_e profile, however, there is no such sharp increase, and it is almost flat in the radial direction. In the detached phase shown in figure 3(*f*), T_e at the flattening region decreases down to <20 eV, which enhances the impurity radiation significantly due to the temperature dependence of the cooling rate function. This is the reason for the enhanced radiation with RMP as observed in figure 2(*g*). It is also noted that a steep gradient appears in n_e as well as in T_e in the detached phase. This results in the formation of ETB at the detachment onset, as seen in the steep pressure profile in figure 3(*g*). Although the mechanism of the ETB formation at the detachment onset is not yet clear, the shear flow of the parallel flow is one possible candidate. In the numerical simulation on detachment with an edge magnetic island [19], parallel flow along the separatrix is observed at the detachment transition. This flow is developed in order to supply particles to the *X*-point of the

island, where density condensation occurs due to the *X*-point cooling by a thermal instability. The typical flow speed of order of 10^4 m s^{-1} within the channel width of several centimetres around the separatrix provides a shear flow of several hundreds kHz, which is large enough to suppress the turbulence. Such a mechanism due to parallel shear flow is also discussed in a theoretical model [20, 21]. More careful analysis is left for future work.

In the case without RMP, there is no such steep gradient developed in either T_e or n_e, as shown in figure 3(*a*). At the collapsing phase, figure 3(*b*), the gradient becomes large in both T_e and n_e, but the radial locations are different from each other. The pressure profile becomes steeper at the collapsing phase, as shown in figure 3(*c*), but the gradient is still weaker than the case with RMP (figure 3(*g*)). These results show that the change of the edge magnetic field structure with RMP application leads to a significant difference in the plasma characteristics in various aspects, such as the attainable density range, radiated power, plasma stored energy, stability of detachment, as well as the formation of ETB.

The core energy transport has been analysed with TASK3D [22]. The results are plotted in figure 4 for different line averaged densities. The TASK3D has been updated to be capable of actual density and temperature profiles rather than polynomial fit, as conducted in the previous study [11]. Thanks to this new feature of the code, a more detailed structure of the transport can be obtained than before, such as ETB. As shown in figure 4, the pressure profiles are more peaked at the central region during the detached phase in the case with
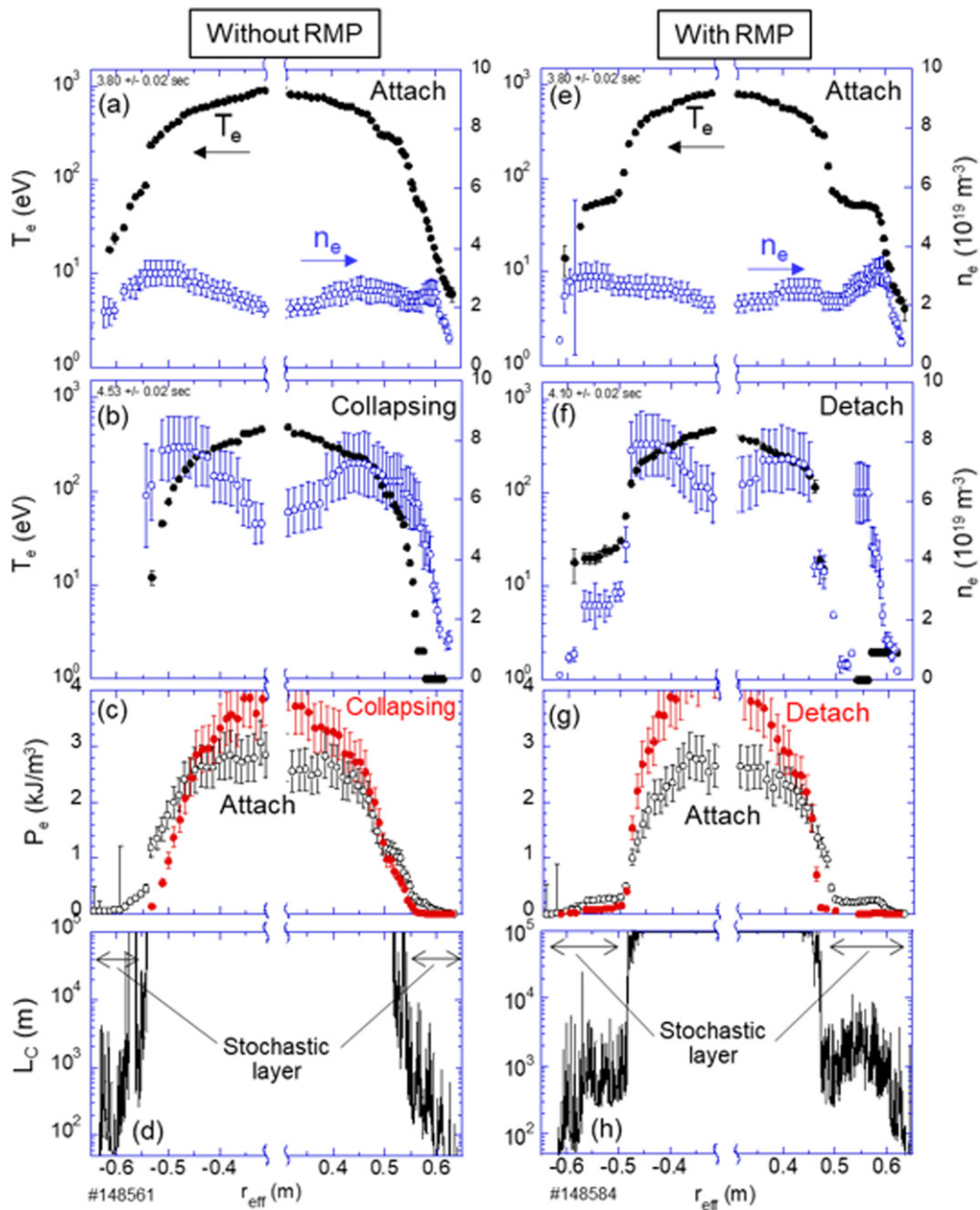
Figure 3. (*a*), (*b*), (*e*) and (*f*) Radial profiles of T_e (black closed circles) and n_e (blue open circles). (*a*) and (*e*): 3.0×10^{19} m^{-3}, (*b*) and (*f*): 6.6×10^{19} m^{-3}. (*c*) and (*g*) Radial profiles of P_e at attached phase (black closed circles) and at collapsing/detached phase (red closed circles), corresponding to (*a*) and (*e*) for attached phase and to (*b*) and (*f*) for collapsing/detached phase, respectively. (*d*) and (*h*) Radial profiles of magnetic field connection length, L_C. Left column: without RMP (#148561), right column: with RMP (#148584). The timings of each plot are as follows: (*a*) 3.80 s, (*b*) 4.53 s, (*c*) attach: 3.80 s. Collapsing: 4.53 s, (*e*) 3.80 s, (*f*) 4.10 s, (*g*) attach: 3.80 s, detach: 4.10 s. (Data from deuterium plasmas.)

RMP. This is mostly due to the deeper penetration of NBI heating with RMP in the detached phase, as shown in figure 4(*e*). The deeper penetration of NBI is caused by shrinkage of the plasma volume by edge cooling during the detachment with RMP. The minor radius of the plasma column is ∼0.50 m with RMP while it is 0.55 m without RMP, as seen in figures 4(*a*) and (*d*) (and figures 3(*c*) and (*g*)), respectively. A clear ETB is confirmed in the pressure profile steepening at the edge of $r_{\text{eff}} = 0.46$–0.48 m with RMP. The transport coefficient, χ_{eff}, decreases in the detached phase in the entire region with RMP

application, as seen in figure 4(*f*). But the level of the transport is almost the same with and without RMP in the core region except for the detailed structure. At $n_e = 6.5 \times 10^{19}$ m^{-3} without RMP, χ_{eff} decreases significantly in the whole radius. This cannot, however, be sustained in the steady state, since this occurs only transiently during the collapsing phase. A rather remarkable difference appears at the ETB region at $r_{\text{eff}} = 0.46$–0.48 m with RMP, where χ_{eff} with RMP decreases by a factor of 2 compared to without RMP. The transport analysis reveals that the difference in core plasma confinement between
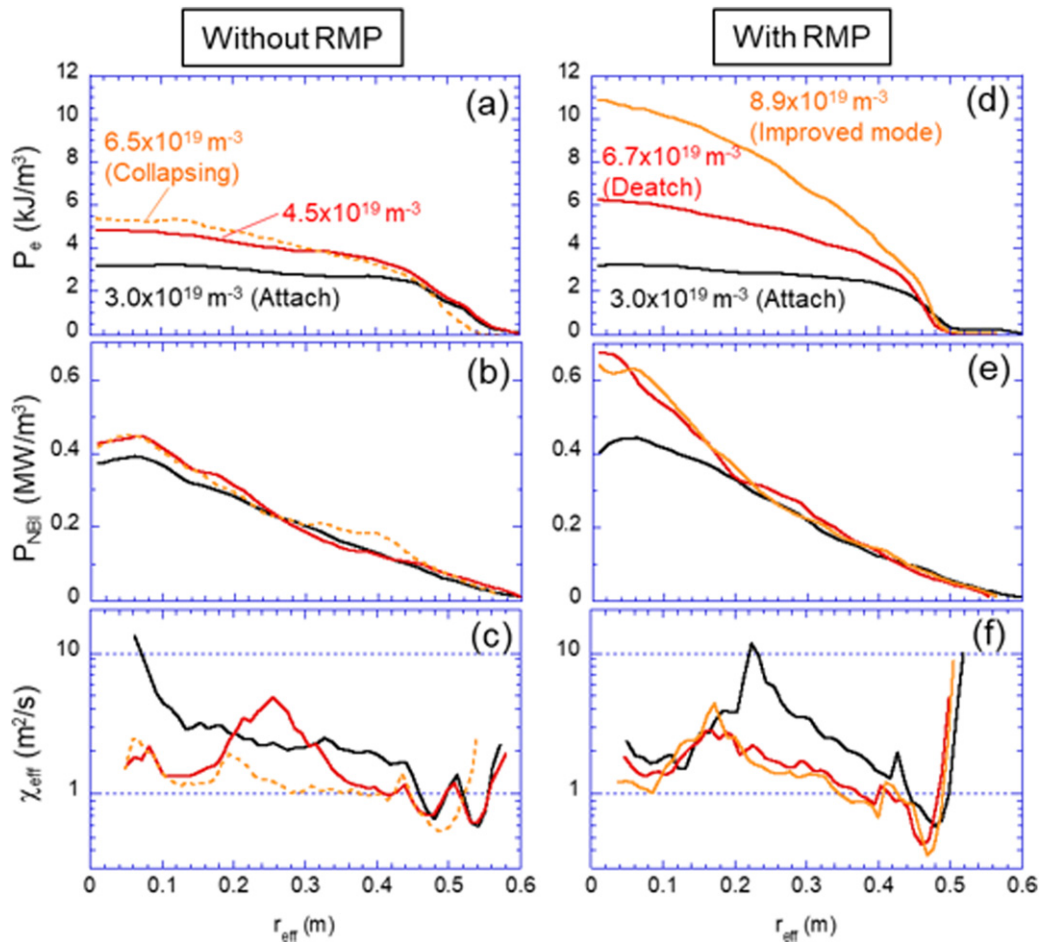
Figure 4. Radial profiles of (*a*) and (*d*) electron pressure, (*b*) and (*e*) NBI heating deposition, (*c*) and (*f*) energy transport coefficients $\chi_{\text{eff}} = 0.5(\chi_e + \chi_i)$ for different densities. Left column; without RMP, right column: with RMP. (Data from deuterium plasmas.)

the cases with and without RMP, as observed in figure 2, is attributed to the change in the transport at the edge region caused by the sharp boundary in the RMP application. The transport analysis also shows that there is no significant degradation of the core transport during the detachment. The results are similar to those in hydrogen plasmas with RMP [11].

3. Confinement mode transition during detached phase with RMP in deuterium plasmas

3.1. Interplay between core plasma transport, ETB and MHD mode excitation

The confinement mode transition during the detached phase with RMP has been observed in several shots and is discussed in more detail in this section. Figure 5 shows the temporal evolutions of the radial profile of T_e, a spectrogram of the magnetic probe signal, the pressure gradient at the ETB region, plasma stored energy (W_p), the time derivative of W_p, dW_p/dt, and the density fluctuation measured with 2D phase contrast imaging (PCI) [23], respectively. As seen in W_p, and dW_p/dt, there is a discontinuous increase in W_p at the detachment transition at 3.95 s. ETB is formed at the confinement boundary, as discussed in the previous section (figure 3(*e*)). A similar

increase in W_p at the detachment transition was also observed in hydrogen plasmas [24]. The increment is, however, larger in deuterium plasmas. The pressure gradient starts increasing, and the density fluctuation starts decreasing (figures 5(*c*) and (*f*)) as a clear indication of the confinement mode transition. However, T_e at the edge region continues to decrease due to the increasing radiation as the detachment deepens (figure 5(*a*)). This lowering T_e and increasing pressure gradient leads to excitation of the resistive pressure gradient-driven MHD mode, which is observed as coherent magnetic fluctuation around 4 kHz with $m/n = 3/3$, starting at 4.15 s, as seen in figure 5(*b*). Since the ETB is developed at the inner edge of the remnant magnetic island of $m/n = 1/1$, the MHD mode of $m/n = 3/3$ is considered to be driven by the pressure gradient at the ETB. The reason why the mode has a higher mode number than the RMP is not yet clear. Once this mode appears, the pressure gradient drops by a factor of 2 and the increase of W_p stops.

Figure 6 shows the temporal evolution of the energy transport coefficients at different radii, ρ. Here ρ is defined as r_{eff}/a_{99}, where a_{99} is a radius of the cylindrical volume that contains 99% of the total stored energy. When the ETB degrades by the MHD mode excitation, the core transport responds to compensate for the degradation of the ETB, that is, χ_{eff} at
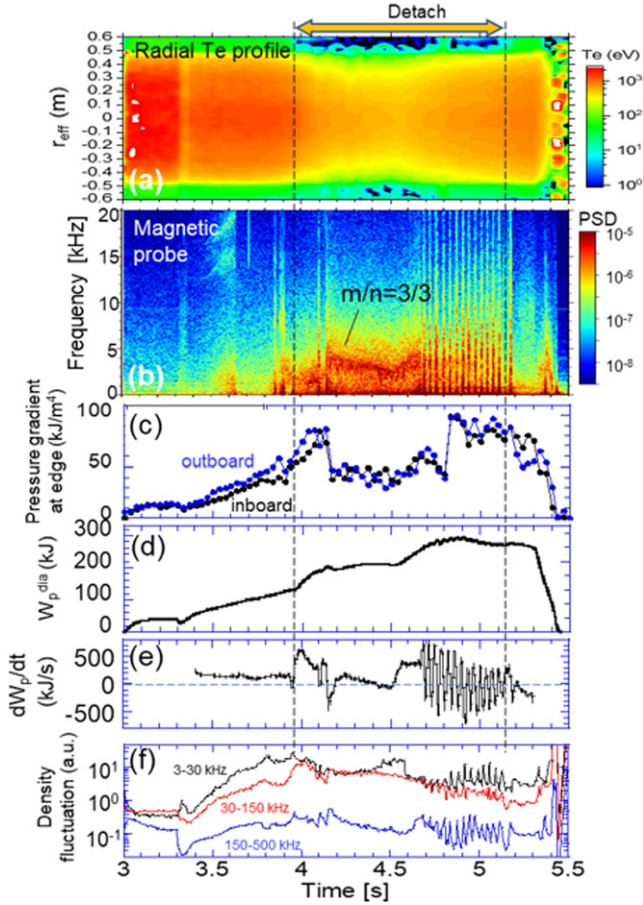
Figure 5. Temporal evolutions of (*a*) radial profile of T_e, (*b*) spectrogram of magnetic probe signal, (*c*) pressure gradient at ETB, (*d*) plasma stored energy (W_p), (*e*) time derivative of W_p, dW_p/dt, (*f*) density fluctuation intensity, with RMP application. (Data from deuterium plasmas.)

$\rho = 0.1$–0.2 and 0.5–0.6 decreases while χ_{eff} at ETB increases. The behaviour clearly shows core-edge coupling of transport. Due to the core transport response, W_p is maintained despite the collapse of the ETB. Similar phenomena have been observed in the impurity seeding experiments in various tokamaks, ASDEX-Upgrade, EAST, and DIII-D, where the plasma stored energy was maintained or core transport improves while the pedestal top pressure (ETB) degrades [25, 26]. During the MHD mode excitation, the density fluctuation with frequency <30 kHz gradually increases, as seen in figure 5(*f*). Then, a sudden increase of W_p sets in at 4.5 s, as seen in figure 5(*d*); at the same time, spin up of the MHD mode frequency in figure 5(*b*) and recovery of the pressure gradient at the ETB in figure 5(*c*) are observed. ELM-like activity starts at 4.7 s, as shown in the burst in the spectrogram of magnetic fluctuation, which hinders the recovery of ETB transiently. The energy loss by the ELM-like burst is about 10 kJ per burst. At 4.8 s, finally the ETB recovers completely, then the density fluctuation is suppressed in all frequency ranges, as shown in figure 5(*f*). The coherent MHD mode ceases and is replaced with the ELM bursts. The energy confinement time increases by 38% compared to before the transition.
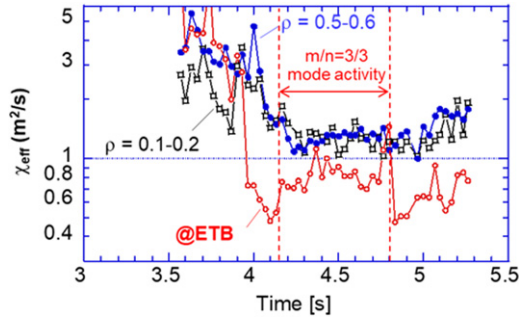

Figure 6. Time traces of χ_{eff} at different radii, at ETB (open circles) averaged over $\rho = 0.1$–0.2 (open squares), 0.5–0.6 (closed circles), respectively. $\rho = r_{eff}/a_{99}$. (Data from deuterium plasmas.)

Shown in figure 7(*a*) is the evolution of n_{eped} and T_{eped} at the pedestal top during the discharge. At the attached phase, the pedestal is in the low density and high temperature regime, i.e. $\nu_{ei}^* \sim 1$. With an increase in density during the density ramp up toward the detachment onset, the temperature decreases while pressure is kept nearly constant. After the detachment, the transition pressure increases due to the ETB formation. The degradation of ETB due to the MHD mode excitation leads to a drop in pedestal pressure. In the figure, it is found that the pressure drop is mainly caused by the drop of T_{eped}, while n_{eped} is kept at the same level. Then, once the confinement mode transition sets in at 4.5 s, the transition proceeds with increasing T_{eped}, resulting in recovery and further development of the pedestal pressure. This behaviour is different from the usual H-mode transition observed in tokamaks and stellarators, where a predominant density increase is observed at the transition [8, 27–30].

Figure 7(*b*) shows the energy confinement time scaled with gyro-Bohm scaling as a function of line-averaged density that is normalized by the density limit. Without RMP, the degradation of the global confinement is significant with increasing density. This is due to the increasing radiation. In the case with RMP application, the confinement degradation with increasing density is modest compared to the case without RMP. It is found that the transition from the attached to detached phase is smooth in terms of the scaling. The confinement mode transition during the detached phase ($t > 4.5$ s) occurs around the density limit, which is shown by orange diamonds. The symbols deviate significantly from the scaling, which is, therefore, a clear indication of confinement improvement.

In order to obtain deeper insight into the relevant physics for the confinement transition as well as the operation limit near the density limit accompanied by strong edge radiation, the adiabatic parameter (α_{adi}) and diamagnetic parameter (α_{dia}) are evaluated at the pedestal top for different phases, that is, ETB formation, degradation of ETB and radiative collapse. α_{adi} is a measure of the adiabaticity; below unity of the parameter, the drift wave turbulence transport is enhanced. It is defined as $\alpha_{adi} = k_\parallel^2 v_{th}^2/(\nu_{ei}|\omega|)$, where v_{th} and ν_{ei} are the thermal velocity of the electron and electron–ion collision frequency. $k_\parallel = 1/(\pi R q)$ and $|\omega| = 10$ kHz is used as a drift wave frequency of the dominant mode based on the density fluctuation
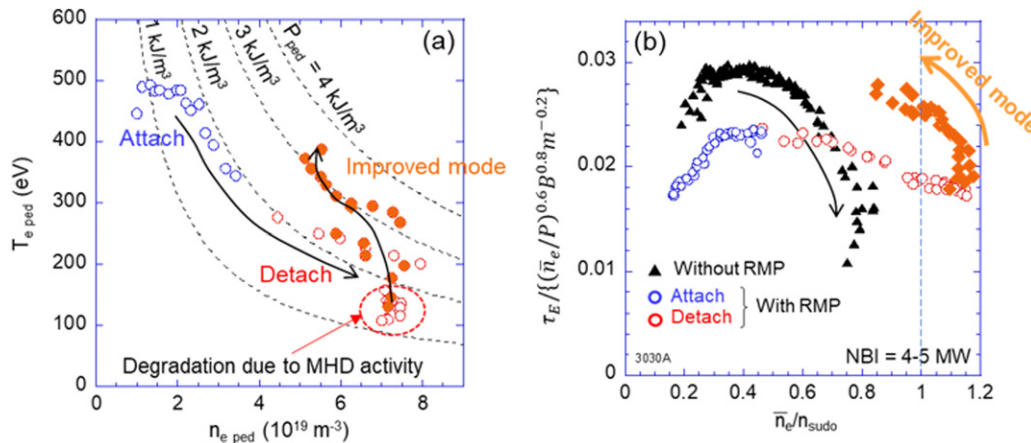
Figure 7. (*a*) Evolution of n_{eped} and T_{eped} at pedestal top during the discharge with RMP, (*b*) energy confinement time scaled with gyro-Bohm scaling as a function of line-averaged density, which is normalized with density limit. Blue circles: attached phase with RMP, red circles: detached phase with RMP, orange diamonds: improved mode with RMP (detach), black triangles: without RMP. (Data from deuterium plasmas.)

spectrum measured by PCI. α_{adi} is a ratio of the parallel electron diffusion rate and turbulence propagation speed of the dominant mode. α_{dia} is a measure of transport enhancement by resistive MHD instability with respect to those with drift wave turbulence. The former transport becomes significant with lower values of α_{dia}. $\alpha_{\text{dia}} = (R/2L_n)^{0.25}\sqrt{D_{\text{gB}}/D_{\text{DRB}}}$, where $L_n, D_{\text{gB}}, D_{\text{DRB}}$ are density gradient scale length, transport coefficients of gyro-Bohm type diffusion, and of the drift resistive ballooning mode, respectively. $D_{\text{gB}} = c_s \rho_i^2/L_n$ and $D_{\text{DRB}} = (2\pi q)^2 \rho_e^2 \nu_{\text{ei}} R/L_n$, where c_s, ρ_i, ρ_e are sound speed, Larmor radius of ion and electron, respectively [31, 32]. α_{dia} is interpreted as a ratio of drift wave frequency and resistive ballooning mode growth rate.

The parameters α_{adi} and α_{dia} evaluated at the pedestal top are plotted in figure 8, where data points were obtained from several shots, including radiation collapse during detachment. It is found that the ETB degradation occurs with $2 < \alpha_{\text{adi}} < 30$ and $1 < \alpha_{\text{dia}} < 40$, still far above unity. This is in clear contrast to the results in [33], where the confinement degradation occurs at $\alpha_{\text{adi}} \lesssim 1$. As for the diamagnetic parameter, the theoretical analysis in [2] suggests that degradation occurs at $\alpha_{\text{dia}} < 0.6$. The absolute value may not be taken seriously due to the simplification of the physics model as well as the scatter in the experimental data. Nevertheless, the relatively large value of α_{adi} (as well as α_{dia}) may be interpreted as the reason for the possibility of the the ETB recovery, where the ETB branch is potentially maintained in the bifurcation, despite the excitation of the MHD activity that forces the system to stay at the L-mode branch. It is noted that the overlapping between the ETB and ETB degradation phases is due to hysteresis of the forward and backward transitions of the ETB formation, as a clear indication of the nonlinearity of the physics mechanism.

The collapsing phase indicated by red triangles is located at smaller values of both α_{dia} and $\alpha_{\text{dia}} \lesssim 2$. The result implies that both the physics processes represented by the parameters

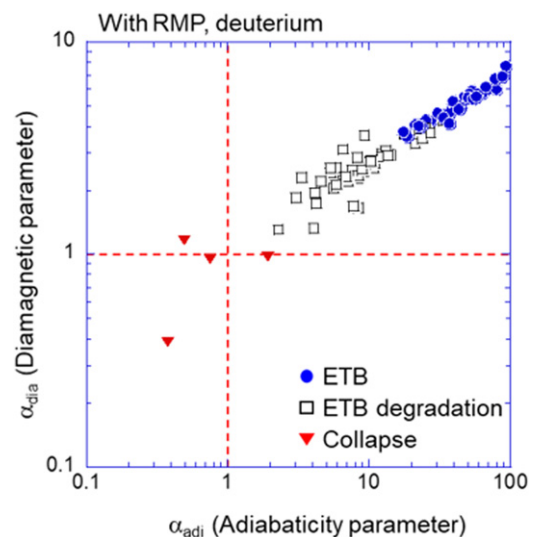**Figure 8.** Evaluation of α_{dia} and α_{adi} at pedestal top for different phases. Closed circles: ETB phase, open squares: ETB degradation phase, triangles: collapsing phase, respectively. With RMP application. (Data from deuterium plasmas.)

are responsible for the operation limit. Indeed, during the collapsing phase, both the density fluctuation and magnetic fluctuation increase significantly. The picture is similar to those discussed in [1, 2, 33].

The series of the evolution in edge temperature, pressure gradient, density fluctuation, and confinement mode transition with ETB formation during detachment provide important insight into the interplay between cold edge plasma and core confinement.

3.2. Impurity decontamination and divertor heat load distribution

The impurity emission intensity and profile were measured with vacuum ultra violet/extreme ultra violet (VUV/EUV) spectroscopy, which views the entire plasma from the outboard
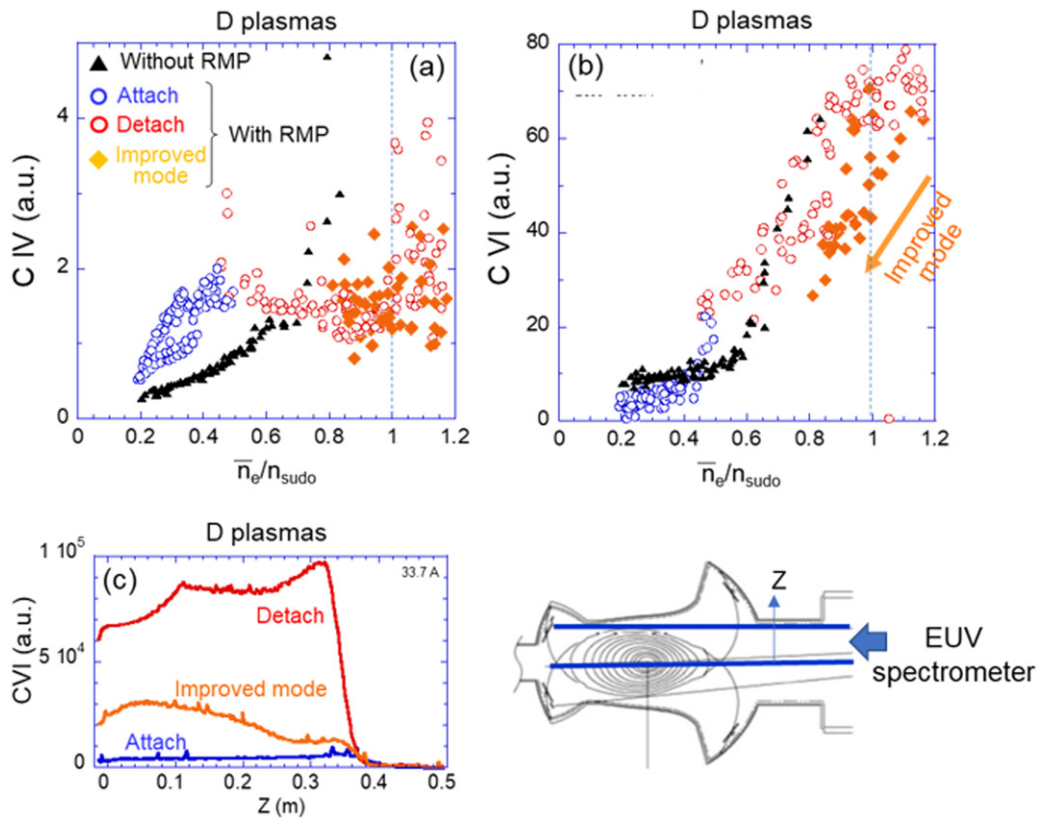
Figure 9. (*a*) and (*b*) Carbon emission intensity as a function of line-averaged density normalized by density limit. (*a*) CIV ($1s^2 2s - 1s^2 2p$, 154.8 nm), (*b*) CVI ($1s-2p$, 3.4 nm). Black triangles: without RMP, blue circles: attached with RMP, red circles: detached with RMP, orange diamonds: improved mode (detach) with RMP. (*c*) Profiles of CVI intensity at different timings. The viewing area of the measurement is shown in the bottom right figure. (All data are from deuterium plasmas.)

side [34, 35]. Figures 9(*a*) and (*b*) show the CIV ($1s^2 2s - 1s^2 2p$, 154.8 nm) and CVI ($1s-2p$, 3.4 nm) intensity as a function of line-averaged density normalized by the density limit. CIV intensity is enhanced by RMP application compared to the case without RMP in the attached phase. This is considered to be due to the increased volume of the low T_e region at the widened stochastic layer. The enhanced impurity emission triggers the detachment transition at $\overline{n}_e / n_{sudo} \sim$ 0.5. During the detached phase, including the improved mode, the CIV intensity remains high. The rapid increase in CIV at $\overline{n}_e / n_{sudo} \sim 0.7$ without RMP is caused by the radiation collapse. CVI intensity is suppressed during the attached phase by RMP application compared to the case without RMP. This is considered to be due to the impurity screening effect with the increased edge stochastic layer width [36–39]. But just before the detachment transition, CVI starts to increase and in the detached phase, a significant increase is observed. This may indicate the impurity penetration into the confinement region during the detached phase. The overall behaviour of CIV and CVI is similar to those in hydrogen plasmas as reported in [11], except for the improved mode, which is not clearly identified in the hydrogen case yet. More detailed comparison between deuterium and hydrogen plasmas is made in section 4.

As the plasma enters the improved mode, the CVI intensity decreases by a factor of 3. The results indicate impurity

decontamination during the improved mode. Similar decontamination was observed in the H-mode phase in W7-AS [40]. This may be partly due to the ELMs during the improved mode, which can expel the impurity in the core region, while the detailed mechanism is not yet clear. The line integrated profiles of the CVI intensity are plotted in figure 9(*c*) at different phases. After the detachment transition, the intensity increases in the entire region with a slightly hollow profile, while during the improved mode, the intensity decreases in the entire region with a slightly peaked profile. The decontamination leads to a decrease in the radiated power to a certain extent, as shown in figure 2(*g*). The radiated power estimated by the resistive bolometer is 50%–60% of the NBI power during the detached phase at maximum, then decreases down to 30%–40% during the improved mode. Since the core plasma is substantially collisional during the detached phase, we expect turbulence may play important role rather than the neo-classical effect. The impact of turbulence on the impurity transport has recently been discussed in [41, 42]. To clarify the mechanism of the decontamination, turbulence transport analysis with a gyrokinetic simulation should be undertaken.

Divertor heat load was measured with 280 channel-Langmuir probe arrays installed at the inboard side divertor plates distributed in the toroidal sections. There are two divertor arrays rotating in helical direction around the torus. They
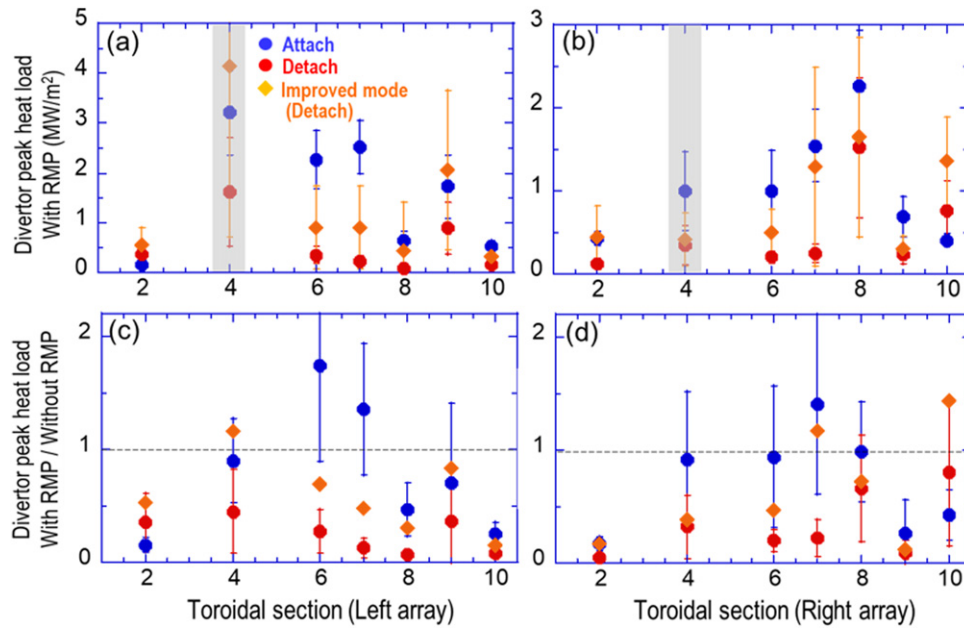
Figure 10. Toroidal profiles of peak divertor heat load with RMP application (*a*) left divertor array, (*b*) right divertor array (see description in the main text). The values at the hatched sections (4L and 4R) should not be compared to those in other sections because of the different shape of the divertor tiles. (*c*) and (*d*) The heat load is normalized with those in the attached phase without RMP application in order to see the effects of RMP on toroidal modulation. Blues circles: attached phase (averaged over 3.7–3.9 s), red circles: detached phase (averaged over 4.4–4.6 s), orange diamonds: improved mode (detach) (averaged over 4.9–5.1 s). (Data from deuterium plasmas (#148584).)

are called the left and right array, respectively, according to the location at the inboard midplane viewed from the outboard side. Figures 10(*a*) and (*b*) show the toroidal profile of the peak divertor heat load with RMP application at three timings: attached, detached phases and improved mode. The toroidal section 4, which is hatched in figures 10(*a*) and (*b*), has different shaped divertor tiles where the incident angle of field lines is larger than the other tiles. Therefore, the absolute values at this section should not be compared with those in the other sections. In the attached phase (blue circles), there is a clear $n = 1$ mode structure in the toroidal direction, which is due to the mode structure of the RMP field. In the detached phase (red circles), the peak divertor heat load decreases in most of the sections, except for section 2L and 10R. In these sections, the peak heat load slightly increases during the detached phase, although the heat load is already suppressed during the attached phase due to the toroidal modulation by the RMP. During the improved mode in the detached phase (orange diamonds), where the heat load is averaged over inter- and ELM pulse periods, the heat load increases in all sections compared to the period before the transition. Nevertheless, in most of the sections, the heat load is still lower than those in the attached phase, except for sections 2L, 9L, 2R, and 10R. The increase of the heat load during the improved mode is partly due to the decreased radiated power as observed in figure 2(*g*), which is caused by impurity decontamination during the improved mode, as described above. The toroidally asymmetric increment of the heat load during the improved mode is considered due to the MHD burst that would eject the filament structure transported towards the divertor plates.

The divertor heat load profile in the toroidal direction has slight toroidal asymmetry, even without RMP application, which is probably attributed to the misalignment of the tiles as well as to the different history of the erosion of individual probe tips. In order to extract the effects of RMP application on the toroidal modulation of the divertor heat load pattern, the heat load is normalized by those without RMP during the attached phase and is plotted in figures 10(*c*) and (*d*) (in this plot, section 4 can be compared to the other sections). In the attached phase, an $n = 1$ mode structure appears in the profile, where the heat load at sections 6 and 7 of the left array (6L, 7L) and sections 7 and 8 of the right array (7R, 8R) is almost the same or higher than the case without RMP. The heat load at other sections is lowered with RMP. This is similar to the observation in hydrogen plasmas [11]. In the detached phase, the heat load decreases at most of the sections except for section 2 of the left array (2L) and section 10 of the right array (10R), where the heat load slightly increases. Nevertheless, they are still lower than those in the attached phase without RMP. This is also similar to the behaviour in the hydrogen plasmas [11]. The heat load reduction is larger than the hydrogen plasmas. This is considered to be due to the higher radiated power caused by the increased carbon amount in the deuterium plasmas than the hydrogen plasmas because of the higher chemical and physical sputtering rate of the graphite divertor plates. The magnetic footprint at the divertor plates was traced by a field line tracing code assuming vacuum magnetic configuration, which is a good approximation in low beta plasma (0.34%) in the present experiments. It is found that the flux tube at the section where the heat load increases during the detached phase (2L and 10R) tends to travel near the O-point of the $m/n = 1/1$ island created by the RMP, while the others
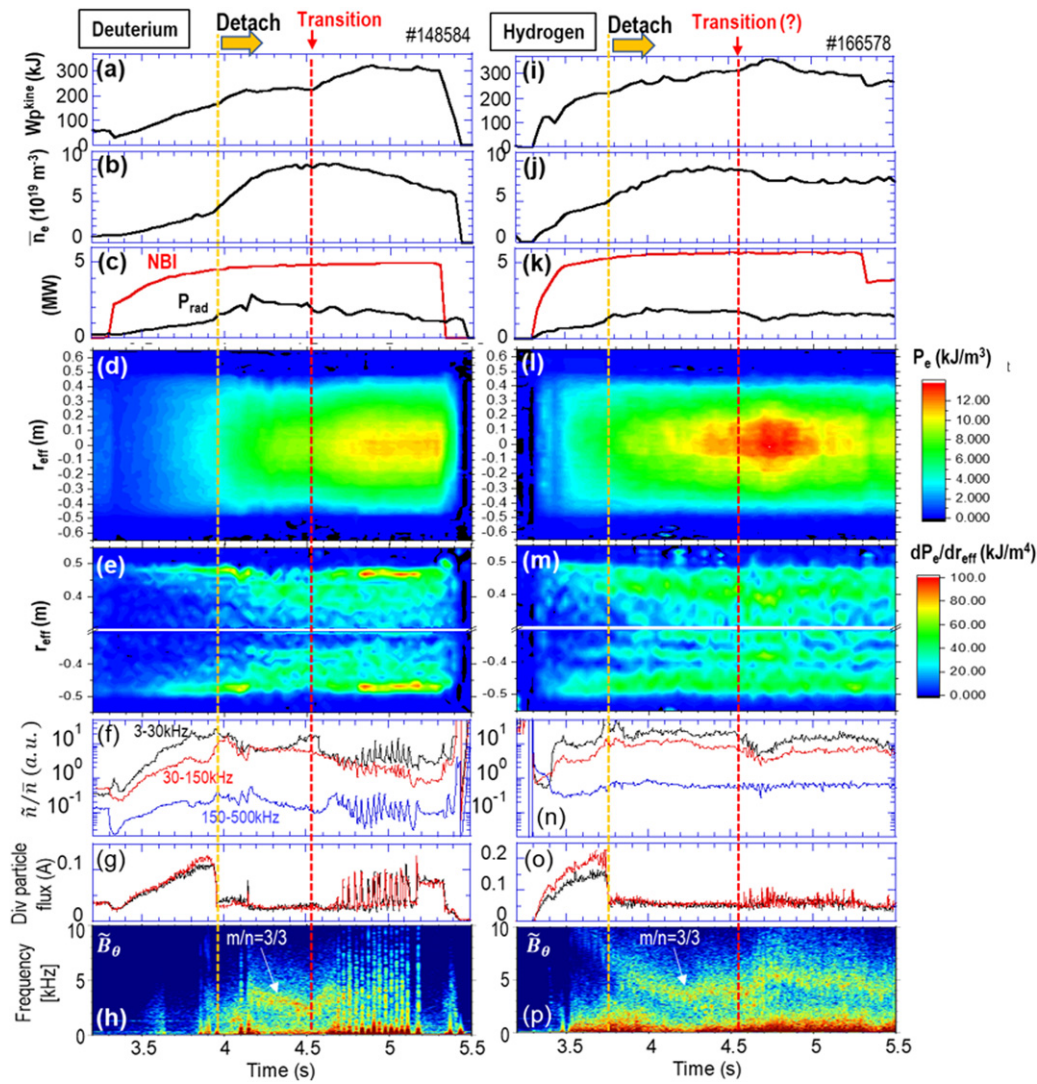
Figure 11. Time traces of plasma parameters for deuterium (*a*)–(*h*) and hydrogen (*i*)–(*p*) plasmas. (*a*) and (*i*) plasma stored energy (kinetic), (*b*) and (*j*) line-averaged density, (*c*) and (*k*) NBI heating and radiated power, (*d*) and (*l*) radial profile of electron pressure, (*e*) and (*m*) radial profile of pressure gradient, (*f*) and (*n*) density fluctuation measured by PCI, (*g*) and (*o*) divertor particle flux, (*h*) and (*p*) spectrogram of magnetic fluctuation. (Data from deuterium: #148584, hydrogen: #166578.)

are further away from the *O*-point or connected near the *X*-point of the island. The decrease of the divertor heat load in the detached phase is ∼70% on average in the toroidal direction, while the radiated power is 50%–60% estimated from the bolometer. There is still a 10%–20% discrepancy between the two measurements.

During the improved mode, the heat load increases in most of the sections, but still stays lower than those in the attached phase without RMP, except for sections 4L, 7R, and 10R. Further reduction of the heat load during the improved mode will be tried in the next experiments by auxiliary impurity seeding, such as Ne.

4. Comparison between deuterium and hydrogen plasmas

Figure 11 shows the temporal evolutions of various plasma parameters of detachment discharges with RMP application in

deuterium and hydrogen plasmas. The density was ramped up in a similar way in both cases in order to investigate the difference between the isotopes. In the deuterium case, the total NBI (deuterium beam) heating power was 5 MW with 3.6 MW in the co-direction and 1.4 MW in the counter-direction, and the purity of the plasmas was D/(D + H) ∼ 100%. In the hydrogen case, the total NBI (hydrogen beam) heating power was 5.7 MW with 3.4 MW in the co-direction and 2.3 MW in the counter-direction, and the purity was D/(D + H) ∼ 30%. The toroidal magnetic field direction is counterclockwise seen from the top of the torus. It is noted that the hydrogen discharges in the present analysis are different from those in [11], where the toroidal magnetic field direction was opposite to the present case, that is, clockwise seen from the top of the torus, and the NBI heating was 2.5 MW in the co-direction and 4.3 MW in the counter-direction, respectively (injection energy was ∼140 keV).
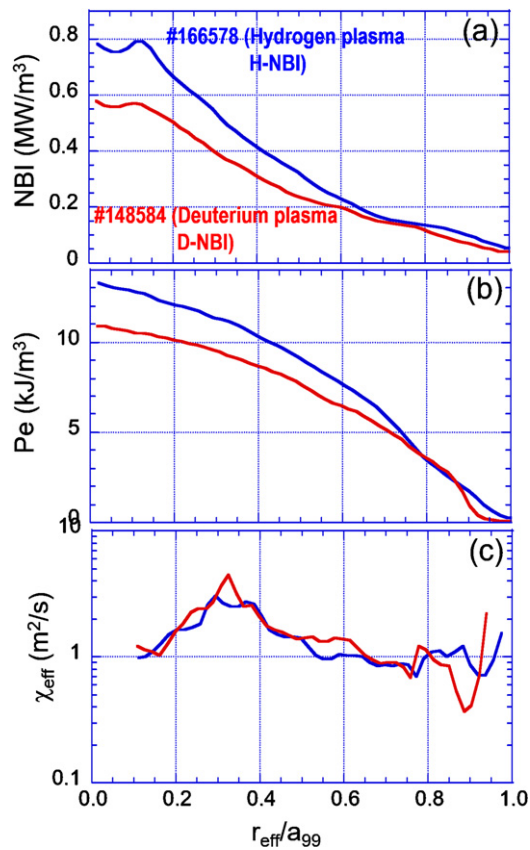
Figure 12. Radial profiles of (*a*) NBI heating deposition, (*b*) electron pressure, (*c*) heat transport coefficient for hydrogen (blue) and deuterium (red) plasmas. NBI heating deposition and the heat transport coefficient were obtained by the TASK-3D code. Deuterium: #148584 at 4.90 s, hydrogen: #166578 at 4.70 s, where W_p reaches maximum, respectively.

Figure 13. Radial profiles of (*a*) electron temperature, (*b*) electron density, (*c*) electron pressure for hydrogen (blue) and deuterium (red) plasmas. Deuterium: #148584 at 4.90 s, hydrogen: #166578 at 4.70 s, where W_p reaches maximum, respectively. The ETB region at $r_{eff} = +/-0.47-0.48$ m corresponds to the inner edge of the stochastic layer (see figure 3(*h*))

In the hydrogen case, the detachment transition occurs at 3.75 s, as seen in the reduction of the divertor particle flux in figure 11(*o*). The plasma stored energy continues to increase after the transition until $t \sim 4.7$ s, as seen in figure 11(*i*). It is, however, difficult to define the timing of the confinement mode transition such as observed in the deuterium case. The pressure profile evolution in figures 11(*d*) and (*l*) shows a more peaked profile in the hydrogen case than in the deuterium case. This is due to the deeper penetration of the hydrogen beam than the deuterium beam, where the injection energy of the beams is 152–177 keV in deuterium beams and 163–165 keV in hydrogen beams. The radiated power is higher in the deuterium case than in the hydrogen case. This is due to the larger amount of carbon source in the deuterium plasma as typical in the LHD, possibly because of the higher chemical sputtering of carbon by deuterium.

Just after the detachment transition, a slight decrease in the density fluctuation in the 3–30 and 30–150 kHz range is observed in the hydrogen case, as seen in the deuterium case, figures 11(*f*) and (*n*). At $t \sim 4.55$ s, a further decrease in the density fluctuation in the 3–30 and 30–150 kHz range is seen in the hydrogen case, while the fluctuation in the 150–500 kHz range shows no clear change. At this timing, W_p increases
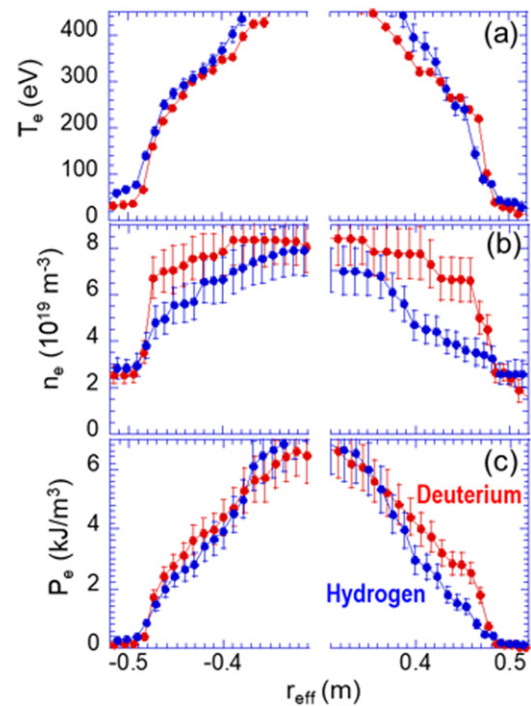
slightly, as seen in figure 11(*i*), which may indicate the confinement mode transition; however, the confinement mode transition is more pronounced in the deuterium case with the clear spontaneous increase in W_p and the reduction of density fluctuation in all frequency ranges. In the hydrogen case, no clear ETB appears or it is weaker than in the deuterium, as seen in the pressure gradient profile in figures 11(*e*) and (*m*). In the divertor particle flux, small and frequent spikes are observed around the reduction of the density fluctuation concomitant with a W_p increase, $t \sim 4.55$ s. These results imply that a strong shear flow may exist or radial electric field shear at the boundary in the deuterium plasma that kills the turbulence and develops the steeper pressure gradient as observed in the data, although no CXS measurements are available at the edge region due to the low temperature, ~ 10 eV. In the spectrogram of magnetic fluctuation, a similar quasi-coherent mode of $m/n = 3/3$ appears during the detachment phase in the hydrogen case, as in the deuterium case. These comparisons show a clear difference in the overall behaviour between the deuterium and hydrogen plasmas in a similar operation scenario, that is, no clear ETB, no clear reduction in high frequency component (150–500 kHz) in the density fluctuation, and no clear confinement mode transition are observed in the hydrogen plasmas.

The results of the transport analysis with the TASK-3D code are shown in figure 12, where the radial profiles of the NBI power deposition, electron pressure, and heat transport coefficients are plotted as a function of r_{eff}/a_{99} for the timing
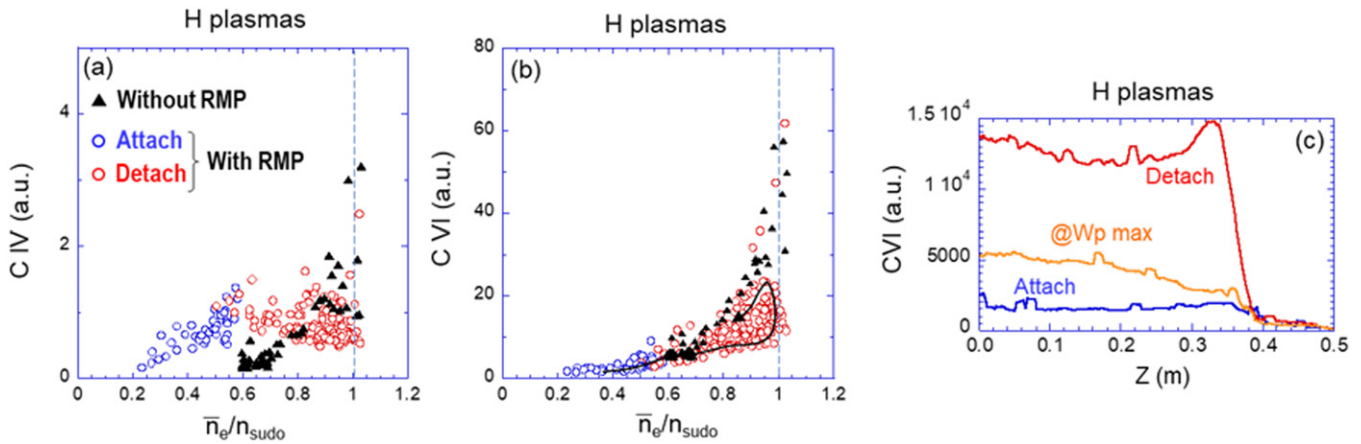
Figure 14. (*a*) and (*b*) Carbon emission intensity as a function of line-averaged density normalized by density limit. (*a*) CIV ($1s^2 2s$–$1s^2 2p$, 154.8 nm), (*b*) CVI ($1s$–$2p$, 3.4 nm). Black triangles: without RMP, blue circles: attached with RMP, red circles: detached with RMP. The arrow in (*b*) shows the sequence of the discharge #166578 (shown in figure 11), where the impurity decontamination takes place. (*c*) Profiles of CVI intensity at different timings. The viewing area of the measurement is shown in figure 9. (All data are from hydrogen plasmas.)

of the peak W_p, 4.90 s for deuterium and 4.70 s for hydrogen cases, respectively. The NBI deposition profile is more peaked in the hydrogen beam due to the deeper penetration as mentioned above, attributed to the lighter mass in the hydrogen with a similar injection energy. This results in the central peaking of the pressure profile in the hydrogen case than the deuterium case. But, at the edge region, a clear ETB is formed in the deuterium plasmas, which is not seen in the hydrogen plasma. Here, the pressure profiles are obtained from the Thomson scattering data by averaging inboard (negative r_{eff}) and outboard (positive r_{eff}) profiles, and used as an input for the TASK-3D analysis. The heat transport coefficient shows an almost similar trend in the core region between the deuterium and hydrogen cases, except for the clear reduction at $\rho \sim 0.9$ in the deuterium case as a consequence of the ETB formation.

The plasma parameter profiles at the edge region obtained from the Thomson scattering system are plotted in figure 13 for deuterium and hydrogen plasmas. A steep gradient is established in T_e in both deuterium and hydrogen plasmas at the inner edge of the stochastic layer, $r_{\text{eff}} = +/-0.47$–0.48 m, as discussed in figure 3(*h*). The density profile also shows an enhanced gradient at the same location, but it is more pronounced in the deuterium plasmas than the hydrogen ones. The resulting pressure profile is more peaked in the deuterium case. The results suggest that the difference in the hydrogen isotope in the ETB formation comes from the particle transport, which is improved more in the deuterium plasmas during the detached phase.

The impurity behaviour is analysed in figure 14, where the intensity of CIV, CVI are plotted as a function of density which is normalized by the Sudo density limit. Figures 14(*a*) and (*b*) of the hydrogen plasmas can be compared to those of the deuterium ones in figures 9(*a*) and (*b*), respectively. Since we have no clear transition timing defined in the case of hydrogen, the data points are divided into two phases with RMP, that is, attached (blue) and detached (red) phases, in addition to the case without RMP (black triangles). The intensity of
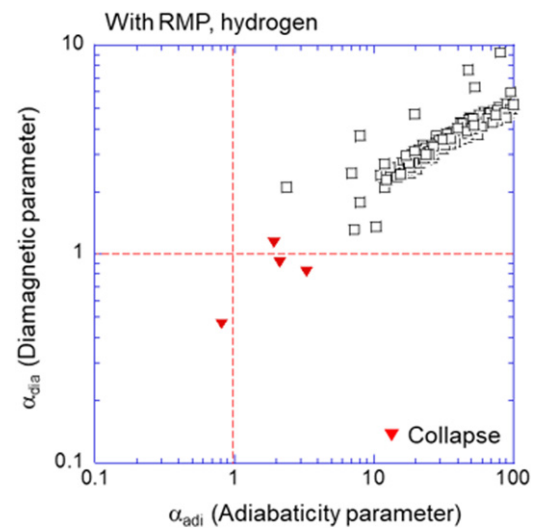

Figure 15. Evaluation of α_{dia} and α_{adi} at pedestal top including collapsing phase for hydrogen plasmas. Red triangles represent collapsing phase. With RMP application.

CIV is roughly half of that in the deuterium case. This is a typical situation in the LHD experiments, and is considered to be due to the larger sputtering (either physical or chemical) yield of carbon from the divertor plates in the deuterium plasmas. The CIV intensity is already larger in the attached phase with RMP than the case without RMP due to enhanced edge radiation, and stays nearly constant during the detached phase. The behaviour is similar to the deuterium case. The CVI intensity is found to be significantly lower in the hydrogen plasmas in the detached phase than in the deuterium by a factor of 3–4. The difference cannot account for the difference in CIV which is as a proxy for the carbon source amount. The higher level of CVI intensity during the detached phase in the deuterium plasmas suggests stronger impurity penetration, which may be attributed to the strong ETB formation in the deuterium case, especially for particle transport, as discussed in figure 13, while the impurity decontamination takes place
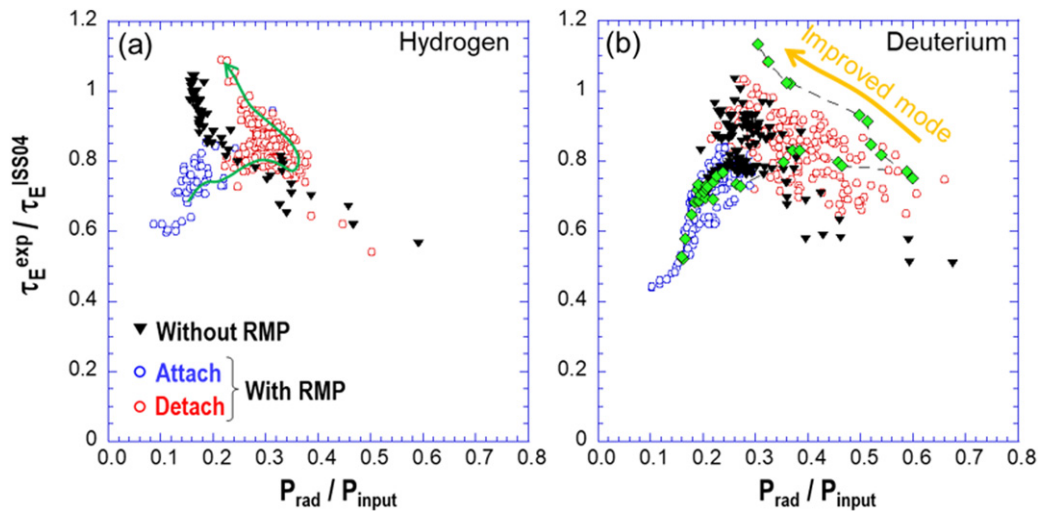
Figure 16. Energy confinement time scaling as a function of radiated power fraction for (*a*) hydrogen and (*b*) deuterium plasmas. Black triangles: without RMP, blue circles: attached phase with RMP, red circles: detached phase with RMP. The green arrow in (*a*) shows the sequence of discharge #166578, green diamonds in (*b*) shows the sequence of discharge #163381.

during the improved mode. Plotted in figure 14(*c*) is a vertical profile of the line integrated CVI emission measured in the EUV spectrometer, as shown in figure 9. The intensity of figure 13(*c*) cannot be compared to that in figure 9(*c*) due to technical reasons, and therefore only the profile shape and temporal evolution are discussed here. It is found that during the detached phase, the CVI intensity increases in the entire radial range, while toward the timing of the maximum W_p the intensity decreases by a factor of about 3. The trace of the black line in figure 14(*b*) shows the time evolution of CVI during the discharge of #166578 (shown in figure 11). Similar to the deuterium plasmas, the impurity decontamination is found in the hydrogen plasmas when the global confinement increases toward its maximum.

he adiabaticity and the diamagnetic parameters are evaluated for the hydrogen plasmas and plotted in figure 15. Although there is no clear pedestal in the case of hydrogen, we have evaluated the parameters at the same radial position as the deuterium case. The plot shows a similar tendency as the deuterium case, except that α_{dia} is systematically smaller than the deuterium case because of the mass dependence, $\alpha_{dia} \propto m_i^{0.25}$. We find that the collapsing phase starts around the time when both α_{adi} and α_{dia} are close to unity as well. It is also found that, despite the range of both parameters reaching same the level as the deuterium case where ETB is formed, that is, $\alpha_{adi} \sim 100$ and $\alpha_{dia} \sim 50$, no ETB is established in the hydrogen plasmas.

The overall performance of the hydrogen and deuterium plasmas for the series of discharges is investigated with energy confinement time scaling in the helical device, ISS04 [43], as a function of the total radiated power fraction with respect to the total heating power, as plotted in figure 16. Without RMP, the confinement degrades as a monotonic function of the radiated power fraction in both hydrogen and deuterium plasmas. With RMP application, the global confinement in the attached phase is worse than the case without RMP. This is due to the edge magnetic island created by the RMP, while the

confinement becomes better with increasing radiated power. In the detached phase, the confinement gradually decreases with radiated power. The degradation is, however, modest in the deuterium plasmas than the hydrogen ones. A trajectory of the transition sequence of the best performance obtained up to the present is indicated with green diamonds in the deuterium plasmas, where the confinement improvement begins after reaching the maximum radiation, proceeds with decreasing radiation, and culminates around $P_{rad}/P_{input} = 0.3$. A trajectory of the typical sequence is also shown in the hydrogen case with an arrow in figure 16(*a*), where it traces a similar shape to deuterium, but is somewhat degenerated in the parameter space. The maximum confinement is reached around $P_{rad}/P_{input} = 0.2$. The whole data points in the deuterium plasma slightly shifted in the higher radiation level than the hydrogen case, which is due to the increased carbon amount, as mentioned above. At the same time, it turned out that the better confinement is sustained in the deuterium plasmas than in the hydrogen ones at a higher radiation level. This may be attributed to the pronounced ETB formation as well as to the larger carbon penetration in the deuterium plasmas, the latter of which could suppress the ITG turbulence, as discussed in [4, 5]. More quantitative analysis to disentangle the effects should be undertaken in future works.

The comparison between the deuterium and hydrogen plasmas shows similar features *qualitatively* in the density and magnetic fluctuations, the impurity behaviour, including the decontamination toward the high confinement phase, and global confinement as a function of radiated power, while quantitatively, most of the features are more pronounced in the deuterium case, and thus the deuterium plasmas exhibit clearer confinement mode transition with clear ETB formation.

5. Summary

The compatibility of divertor heat load mitigation with good core performance is of critical importance for a nuclear fusion

reactor. In general, cold edge plasma tends to degrade core plasma performance due to the degradation of ETB. Theoretical models to describe the deterioration have been proposed. Experimental studies on this issue and comparison with the models still need to be conducted in various magnetic field configurations. In the present experiments in LHD, we have found that the application of RMP significantly changes plasma performance in core confinement and divertor heat load mitigation in deuterium plasmas, that is, plasma stored energy increases with ETB formation in the detached phase, impurity radiation is enhanced with an increased volume of cold edge plasma.

The ETB formation occurs at the detachment transition with RMP. The ETB develops at the inner separatrix of the remanent magnetic island with $m/n = 1/1$ mode induced by the RMP. A possible role of plasma parallel flow along the separatrix for the ETB formation is pointed out, where the flow is driven in the thermal condensation instability as predicted by numerical simulations.

In the detached phase, an interplay between the core plasma transport, including ETB and cold edge plasmas, has been observed as follows. The ETB is degraded as the detachment deepens when the resistive pressure gradient-driven MHD mode is excited. During the ETB degradation, the core transport reduction is observed as a signature of core-edge coupling, then W_p is kept constant despite the ETB collapse. In the meantime, density fluctuation gradually increases, then a spontaneous increase of W_p and recovery of ETB occurs to develop improved core plasma confinement. Then, the coherent MHD mode disappears, being replaced with ELM bursts. The energy confinement time after the transition clearly deviates from gyro-Bohm scaling. The estimated adiabaticity parameter α_{adi} and the diamagnetic parameter α_{dia} at the pedestal top are found to be still far above unity, even during the ETB degradation with the coherent MHD mode excitation.

During the improved confinement mode, impurity decontamination is observed in the EUV spectroscopy measurement of CVI intensity. The toroidal profile of the divertor heat load pattern shows an $n = 1$ mode structure in the toroidal direction in the attached phase with the RMP application, as is similar to that in the hydrogen plasmas. After the detachment transition, the divertor heat load decreases in most of the toroidal sections, while an increase occurs at certain sections. In the improved confinement mode, the heat load increases slightly due to the radiated power reduction caused by the impurity decontamination and to the ELM pulses. Further experiments are planned to attempt to suppress the heat load in the entire toroidal sections.

A comparison between deuterium and hydrogen plasmas shows that the hydrogen plasma exhibits similar features to the deuterium plasmas but some of the features, such as a reduction of density fluctuations, confinement mode transition, and the ETB formation, are more evident in the deuterium plasmas. The impurity decontamination toward highest confinement takes place in both isotopes. It is also found that better global confinement is sustained in the deuterium plasmas at a high radiation fraction >0.4.

The results obtained in the present study provide deeper insight into the physical processes in the nteraction between cold edge plasma and core plasma transport, based on which the compatibility of good core plasma performance and divertor heat load mitigation will be explored in the magnetic configuration with the edge stochastic layer and magnetic island.

ORCID iDs

M. Kobayashi ⬤ https://orcid.org/0000-0002-0990-7093
Y. Hayashi ⬤ https://orcid.org/0000-0001-6090-5010
Y. Takemura ⬤ https://orcid.org/0000-0003-3754-897X
K. Ida ⬤ https://orcid.org/0000-0002-0585-4561
T. Kinoshita ⬤ https://orcid.org/0000-0003-3930-4434
K. Mukai ⬤ https://orcid.org/0000-0003-1586-1084
S. Masuzaki ⬤ https://orcid.org/0000-0003-0161-0938

References

[1] Hajjar R.J., Diamond P.H. and Malkov M.A. 2018 *Phys. Plasmas* **25** 062306
[2] Rogers B.N., Drake J.F. and Zeiler A. 1998 *Phys. Rev. Lett.* **81** 4396
[3] Tokar M.Z. 2003 *Phys. Rev. Lett.* **91** 095001
[4] Tokar M.Z., Osakabe M., Kobayashi M., Mukai K., Nagaoka K., Takahashi H., Tanaka K. and Morisaki T. 2020 *Plasma Phys. Control. Fusion* **62** 075008
[5] Osakabe M. *et al* 2014 *Plasma Phys. Control. Fusion* **56** 095011
[6] Maddison G.P. *et al* 2014 *Nucl. Fusion* **54** 073016
[7] Itoh S.-I. and Itoh K. 1989 *Nucl. Fusion* **29** 1031
[8] Wagner F., Hirsch M., Hartfuss H.-J., Laqua H.P. and Maassberg H. 2006 *Plasma Phys. Control. Fusion* **48** A217
[9] Kobayashi M. and Tokar M.Z. 2019 Experimental studies of and theoretical models for detachment in helical fusion devices *Fusion Energy* (10.5772/intechopen.87130)
[10] Kobayashi M. *et al* 2013 *Nucl. Fusion* **53** 093032
[11] Kobayashi M. *et al* 2019 *Nucl. Fusion* **59** 096009
[12] Pandya S.N. *et al* 2016 *Nucl. Fusion* **56** 046002
[13] Zhang H. *et al* 2017 *Phys. Plasmas* **24** 022510
[14] Narushima Y., Kobayashi M., Akiyama T., Sakakibara S., Masuzaki S., Ashikawa N. and Ohno N. 2013 *Plasma Fusion Res.* **8** 1402058
[15] Takeiri Y. *et al* 2017 *Nucl. Fusion* **57** 102023
[16] Ohyabu N. *et al* 1994 *Nucl. Fusion* **34** 387
[17] Kobayashi M. *et al* 2010 *Phys. Plasmas* **17** 056111
[18] Sudo S., Takeiri Y., Zushi H., Sano F., Itoh K., Kondo K. and Iiyoshi A. 1990 *Nucl. Fusion* **30** 11
[19] Kobayashi M. and Tokar M.Z. 2020 *Contrib. Plasma Phys.* **60** e201900138

[20] Catto P.J. *et al* 1973 *Phys. Fluids* **16** 1719
[21] Sasaki M., Itoh K., Kosuga Y., Dong J.Q., Inagaki S., Kobayashi T., Cheng J., Zhao K.J. and Itoh S.-I. 2019 *Nucl. Fusion* **59** 066039
[22] Yokoyama M. *et al* 2017 *Nucl. Fusion* **57** 126016
[23] Tanaka K. *et al* 2008 *Rev. Sci. Instrum.* **79** 10E702
[24] Kobayashi M. *et al* 2018 *Nucl. Mater. Energy* **17** 137
[25] Kallenbach A. *et al* 2020 Development towards an ELM-free DEMO pedestal radiative cooling scenario in ASDEX Upgrade *EX/2 IAEA FEC 2020* (Nice, France 10-15, May 2021) (https://doi.org/10.1088/1741-4326/abbba0)
[26] Wang L. *et al* 2020 Achievements of actively controlled divertor detachment compatible with sustained high confinement core in DIII-D and EAST *IAEA FEC 2020* (Nice, France 10-15, May 2021) (https://doi.org/10.1088/1741-4326/ac4774)
[27] Manso M.E. 1993 *Plasma Phys. Control. Fusion* **35** B141
[28] Toi K., Ohdachi S., Ueda R., Watanabe K.Y., Nicolas T., Suzuki Y., Ogawa K., Tanaka K. and Takemura Y. 2016 *Plasma Phys. Control. Fusion* **58** 094002
[29] Morita S. *et al* 2006 *Plasma Phys. Control. Fusion* **48** A269
[30] Morita S. *et al* 2007 *Nucl. Fusion* **47** 1033
[31] Guzdar P.N., Drake J.F., McCarthy D., Hassam A.B. and Liu C.S. 1993 *Phys. Fluids* B **5** 3712
[32] Zeiler A., Biskamp D., Drake J.F. and Guzdar P.N. 1996 *Phys. Plasmas* **3** 2951
[33] Hong R. *et al* 2018 *Nucl. Fusion* **58** 016041
[34] Zhang H., Morita S., Oishi T., Murakami I., Huang X. and Goto M. 2016 *Plasma Fusion Res.* **11** 2402019
[35] Dong C., Morita S., Goto M. and Zhou H. 2010 *Rev. Sci. Instrum.* **81** 033107
[36] Kobayashi M. *et al* 2013 *Nucl. Fusion* **53** 033011
[37] Chowdhuri M.B. *et al* 2009 *Phys. Plasmas* **16** 062502
[38] Oishi T., Morita S., Dai S.Y., Kobayashi M., Kawamura G., Huang X.L., Zhang H.M., Liu Y. and Goto M. 2018 *Nucl. Fusion* **58** 016040
[39] Dai S., Kobayashi M., Kawamura G., Morita S., Zhang H.M., Oishi T., Feng Y., Wang D.Z. and Suzuki Y. 2016 *Nucl. Fusion* **56** 066005
[40] McCormick K. *et al* 2002 *Phys. Rev. Lett.* **89** 015001
[41] Ida K. *et al* 2019 *Nucl. Fusion* **59** 056029
[42] Kim K., Kwon J.-M., Chang C.S., Seo J., Ku S. and Choe W. 2017 *Phys. Plasmas* **24** 062302
[43] Yamada H. *et al* 2005 *Nucl. Fusion* **45** 1684